Published in final edited form as:

Cell Rep. 2017 January 03; 18(1): 148–160. doi:10.1016/j.celrep.2016.12.012.

Medial and lateral entorhinal cortex differentially excite deep versus superficial CA1 pyramidal neurons

Arjun V. Masurkar[1,2,*], **Kalyan V. Srinivas**[3], **David H. Brann**[3], **Richard Warren**[3], **Daniel C. Lowes**[3], and **Steven A. Siegelbaum**[3,4,5]

[1]Department of Neurology, Columbia University, New York, NY, 10032, USA

[2]Department of Psychiatry, Columbia University, New York, NY, 10032, USA

[3]Department of Neuroscience, Columbia University, New York, NY, 10032, USA

[4]Department of Pharmacology, Columbia University, New York, NY, 10032, USA

[5]Kavli Institute for Brain Science, Columbia University, New York, NY, 10032, USA

SUMMARY

Although hippocampal CA1 pyramidal neurons (PNs) were thought to comprise a uniform population, recent evidence supports two distinct sublayers along the radial axis, with deep neurons more likely to form place cells than superficial neurons. CA1 PNs also differ along the transverse axis with regard to direct inputs from entorhinal cortex (EC), with medial EC (MEC) providing spatial information to PNs toward CA2 (proximal CA1) and lateral EC (LEC) providing non-spatial information to PNs toward subiculum (distal CA1). We demonstrate that the two inputs differentially activate the radial sublayers and that this difference reverses along the transverse axis, with MEC preferentially targeting deep PNs in proximal CA1 and LEC preferentially exciting superficial PNs in distal CA1. This differential excitation reflects differences in dendritic spine numbers. Our results reveal a heterogeneity in EC-CA1 connectivity that may help explain differential roles of CA1 PNs in spatial and non-spatial learning and memory.

Graphical abstract

Correspondence and Lead Contact: arjun.masurkar@nyumc.org (A.V.M.).

[*] Present address: Department of Neurology and Department of Neuroscience and Physiology, New York University School of Medicine, New York, NY, 10016, USA

AUTHOR CONTRIBUTIONS

Conceptualization, AVM and SAS; Investigation, AVM conducted all electrophysiology and optogenetic experiments, KVS performed two-photon microscopy, DHB contributed immunohistochemistry and viral injections, DHB, RAW and DCL completed morphological tracing; Formal Analysis, AVM, KVS, DHB, RAW, DCL; Visualization, AVM, KVS, DLB, RAW, DCL; Writing – Original Draft, AVM, SAS, KVS, DLB; Writing – Review and Editing, AVM, and SAS; Funding Acquisition, SAS; Resources, SAS

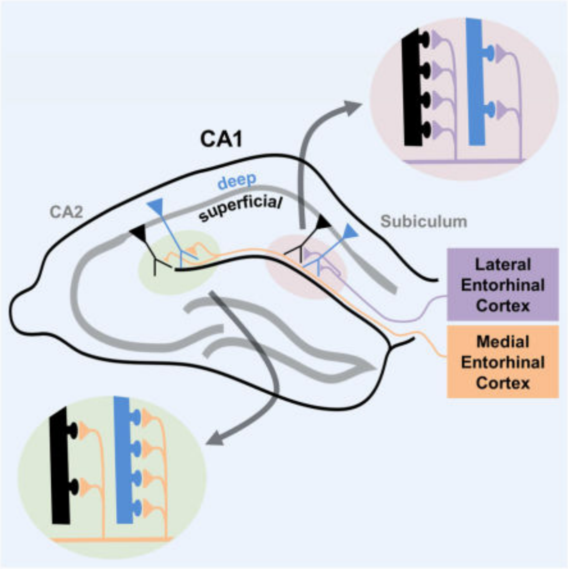

INTRODUCTION

The entorhinal-hippocampal system is a complex network critical for learning and memory guided behaviors in a variety of contexts. Adding to this is the emerging concept that the main output neurons of this network, the hippocampal CA1 pyramidal neurons (PNs), are comprised of a diverse population based on molecular, anatomical, and physiological properties that vary across all three anatomical axes (Slomianka et al., 2011). The *in vivo* relevance of such diversity is unclear but may contribute to the finding that location-dependent (place cell) firing varies along the CA1 radial axis, in that deep layer PNs (closer to stratum oriens or SO) are more likely to form place cells as compared to superficial layer PNs (closer to stratum radiatum or SR) (Mizuseki et al., 2011).

There has been a recent surge of evidence that CA1 PNs are heterogeneous based on anatomic location and non-anatomical features. Physiological differences include variability in neuromodulatory effects (Graves et al., 2012), action potential backpropagation (Golding et al., 2001), and intrinsic excitability across the transverse (Jarksy et al., 2008) and dorso-ventral axes (Dougherty et al., 2012; Malik et al., 2016). CA1 PN diversity is also seen along the radial axis, according to somatic depth, with distinct deep and superficial sublayers based on differences in development (Bayer, 1980), morphology (Bannister and Larkman, 1995; Thome et al., 2014), gene expression (Dong et al., 2009; Cembrowski et al., 2016), modulation by neurotransmitters (Maroso et al., 2016), and projections (Lee et al., 2014; Arszovszki et al., 2014). These sublayers can also be differentiated based on extent of CA2 excitatory drive (Kohara et al., 2014) and the nature of perisomatic inhibition driven by CA3 inputs (Lee et al., 2014; Valero et al., 2015). The differential inhibition may underlie the distinct *in vivo* activity of deep and superficial PNs during sharp wave ripples of sleep and immobility (Stark et al., 2014; Valero et al., 2015).

It is unclear how this diversity contributes to the differential tuning of deep and superficial PNs to different types of information. One possible mechanism is through the functional heterogeneity of the direct entorhinal cortex (EC) input to CA1, with medial (MEC) and lateral (LEC) regions preferentially tuned to spatial versus non-spatial information, respectively (Fyhn et al., 2004; Hargreaves et al., 2005; Deshmukh and Knierim, 2011; Tsao et al., 2013; Igarashi et al., 2014). Anatomical tracing has revealed that direct inputs from MEC and LEC favor distinct zones of CA1 across its transverse axis, with MEC providing dense axonal projections to CA1 closer to CA2 (proximal CA1 or CA1c) and LEC providing input to CA1 closer to subiculum (distal CA1 or CA1a) (Steward, 1976; Wyss, 1981; Tamamaki and Nojyo, 1995; Naber et al., 2001). CA1 PNs in these two regions show different activity-related patterns during spatial and non-spatial tasks in concordance with this cortical input segregation (Henriksen et al., 2010; Burke et al., 2011; Ito and Schuman, 2012; Hartzell et al., 2013; Nakamura et al., 2013; Igarashi et al., 2014).

Given evidence that direct EC inputs play an important role in regulating synaptic plasticity (Dudman et al., 2007; Basu et al., 2013; Basu et al., 2016), spatial representations (Brun et al., 2008; Bittner et al., 2015) and learning and memory (Suh et al., 2011; Kitamura et al., 2014; Basu et al., 2016), a critical question is whether MEC and LEC inputs differentially target deep versus superficial CA1 PNs. We explored this possibility using *in vitro* electrophysiology, two photon microscopy spine imaging, and optogenetics. Our results reveal a circuit architecture in which MEC direct input preferentially excites deep PNs toward CA2, whereas LEC direct input preferentially excites superficial PNs toward subiculum. This provides a potential mechanism for the higher incidence of place cells in deep layers and establishes a framework to gain further insight into EC-CA1 dynamics during spatial and non-spatial learning and memory guided behaviors. These results also show that CA1 PN heterogeneity along the radial and transverse axes are interrelated in that changes along one axis can vary as a function of position along the other axis.

RESULTS

Stronger EC direct excitation, but similar SC excitation, of superficial versus deep PNs in CA1b

We performed *in vitro* whole cell patch clamp recordings from deep and superficial CA1 PNs at different sites along the CA1 transverse axis in acute brain slices from mouse dorsal hippocampus (see Methods). We utilized standard nomenclature (Lorente de Nó, 1934) dividing CA1 into three regions of roughly equivalent length along the transverse axis: CA1a (distal CA1 near subiculum), CA1b (mid-CA1), and CA1c (proximal CA1 near CA2), as delineated in Figure 1A. We first compared deep and superficial PN synaptic properties in mid-CA1 (CA1b), the region most commonly studied, and then examined differences along the transverse axis (Figure 1A, above).

CA1 PNs receive direct input from EC, whose perforant path (PP) projections target CA1 apical dendrites in stratum lacunosum moleculare (SLM), the region furthest from the soma. Input from Schaffer collateral (SC) projections of hippocampal CA3 PNs target CA1 apical dendrites in stratum radiatum (SR), closer to the soma. We investigated whether deep and superficial PNs differed in their excitatory responses to EC or CA3 inputs, using antagonists of $GABA_A$ and $GABA_B$ receptors—2 μm SR95531 and 1 μm CGP55845, respectively—to block inhibition. We measured at the soma the excitatory postsynaptic potentials (EPSPs) evoked by perforant path (PP) and Schaffer collateral (SC) stimulation using increasing strengths of extracellular current delivered by electrodes placed in SLM and SR, respectively (Figure 1A, below). Surprisingly, the PP-evoked EPSP was much larger in superficial versus deep PNs across the entire EPSP input-output curve, with a nearly three-fold higher peak response in superficial PNs (Figure 1B, C; at an 80 V stimulus strength, sPN EPSP = 2.03±0.39 mV; dPN EPSP = 0.77±0.14mV; n=28 each, p<0.0001 by two-way ANOVA). In contrast, SC EPSPs input-output curves showed no significant difference, though there was a trend to slightly larger responses in superficial PNs at high stimulus strengths (Figure 1D, E; at 25 V stimulus strength: sPN EPSP = 7.21±1.3mV; dPN EPSP = 5.99±0.85mV; n=23 each, p=0.18 by two-way ANOVA).

Dendritic spine density and spine number is elevated in SLM of superficial versus deep PNs in CA1b

We next investigated the mechanisms responsible for the three-fold larger PP-evoked EPSP in superficial PNs. As we saw little difference in SC-evoked EPSPs, we reasoned that PP differences were more likely due to synaptic rather than postsynaptic integrative properties, which would affect both SC and PP EPSPs (as borne out by our experimental results showing similar intrinsic properties of deep and superficial PNs, Masurkar et al; unpublished).

We used two photon laser scanning microscopy to quantify dendritic spines as a postsynaptic surrogate measure of excitatory synapses in CA1b superficial and deep PNs filled with 25 μm Alexa Fluor 594 (see Methods). Spine densities were similar in SR oblique dendrites (Figure 2A–C). The superficial PN spine density was equal to 1.46±0.11 spines/μm (451 spines counted on n=13 dendritic segments of average length 24±2 μm, from 4 neurons) and the deep PN spine density was equal to 1.37±0.11 spines/μm (510 spines counted on n=15 dendritic segments of average length 28±3μm, from 4 neurons, p=0.57; sPN and dPN neurons were obtained from 8 slices from 5 animals). Data on individual branches comprising the averages are overlayed. Total spine number was determined by multiplying densities by the average apical dendritic length in SR measured by morphological analysis using biocytin labeling (Figure S1B; n=8 sPN, 8 dPN, see Methods). There was a trend towards a higher number of total spines in SR dendrites of superficial PNs, but this was not statistically significant (Figure 2D; sPN: 3883±812 spines, dPN: 2820±454 spines, p=0.27, individual points from distinct neurons are overlayed). This is consistent with our finding of similar SC EPSPs in the two PN populations (with a trend towards slightly larger responses in superficial PNs).

In these same neurons, we also quantified spine density in SLM, the site of EC inputs. In contrast to SR spine densities, SLM dendrite spine density was two-fold greater in superficial versus deep PNs (Figure 2E–G). Superficial PN spine density was 1.09±0.05 spines/μm (589 spines counted on n=29 dendritic segments of average length 18±1μm, from 4 neurons) whereas deep PN spine density was 0.54±0.04 spines/μm (284 spines counted on n=26 dendritic segments of average length 21±1μm, from 4 neurons, p<0.0001; total data from 8 slices from 5 animals). Data on individual branches comprising the averages are overlayed. Total spine number, derived by multiplying spine density by average SLM dendritic lengths determined by biocytin labeling (Figure S1B, n=8 sPN, 8 dPN, see Methods), was also significantly larger in superficial PNs (Figure 2H; sPN: 1762±274 spines; dPN: 835±226 spines; p=0.02, individual points from distinct neurons are overlayed). This suggests that the three-fold larger PP EPSP in superficial versus deep PNs could be largely explained by a higher number of PP inputs onto superficial PNs.

Preferential EC direct excitation of superficial versus deep PNs in CA1b is accentuated with inhibition intact

Because our initial electrophysiological experiments were performed in the presence of GABA receptor blockers, we next determined if synaptic response differences persist when inhibition is intact, which is more representative of *in vivo* conditions. We therefore measured, in separate experiments, postsynaptic potentials (PSPs) elicited without GABA blockers via extracellular stimulation in SLM and SR (Figure 3A, D). Although PSP peak depolarization evoked by PP stimulation was much smaller in both populations, the striking difference in synaptic responses between deep and superficial PNs persisted, and was even accentuated. With inhibition intact, net PSP depolarization in superficial PNs was now over four-fold greater than that in deep PNs (Figure 3B, C). With a strong (80 V) stimulus, the peak superficial PN PSP amplitude was 0.52±0.21mV (n=17) whereas the deep PN PSP was 0.11±0.05mV (n=18, p=0.0002 by two-way ANOVA). In addition, the net SC PSP was significantly larger in superficial versus deep PNs, unlike when inhibition was blocked (Figure 3E, F). With a 25V stimulus, the peak superficial PN PSP was equal to 6.57±1.01mV (n=23) whereas the peak deep PN PSP was equal to 3.45±0.82mV (n=22, p<0.0001 by two-way ANOVA). This is consistent with findings that deep PNs receive stronger feedforward inhibition, partially mediated by PV+ basket cells, compared to superficial PNs (Lee et al., 2014, Valero et al., 2015).

To compare inhibition elicited by PP stimulation, we measured PSPs before and after application of GABAR blockers, in a subset of the above experiments. We assessed the inferred IPSP by subtracting the PP-evoked EPSP in the presence of GABAR antagonists from the PSP measured with inhibition intact (Figure 4A, B). As expected, in both neurons, GABAR blockade significantly increased the peak depolarizing synaptic response across much of the input-output relation (Figure 4C, D; PSP versus EPSP curves; n=8, p=0.0045 in sPNs; p=0.009 in dPNs; two-way ANOVA), with the superficial PN EPSP significantly greater than the deep PN EPSP (Figure 4C, D; n=8, p<0.0001 by two-way ANOVA). In contrast, there was no significant difference between the inferred PP-evoked IPSPs of superficial and deep PNs (Figure 4E, F; at 80 V, the sPN IPSP = −1.34±0.55 mV and the dPN IPSP = −1.18±0.37 mV; n=8, p=0.12 by two-way ANOVA). As a result, the IPSP/EPSP (I/E) ratio was much greater in deep PNs (Figure 4G, H). With an 80 V stimulating pulse, the superficial PN I/E ratio was 0.90±0.22 whereas the deep PN I/E ratio was 2.62±0.88 (n=8, p=0.0003 by two-way ANOVA).

In principle, inhibition evoked by SLM stimulation could be feedforward, feedback or monosynaptic via direct stimulation of GABAergic axons. Under the conditions of our experiments, the monosynaptic IPSP evoked by SLM stimulation, determined in separate experiments with glutamatergic transmission blocked (50 μm APV and 10 μm CNQX), was very small, less than 10% the size of the inferred IPSP evoked with excitatory transmission intact (Figure S2; at 80V, the sPN IPSP = 0.06±0.06mV and the dPN IPSP = 0.11±0.02mV; n=7, p=0.25 by two-way ANOVA). Moreover, feedback inhibition is unlikely to contribute to the net IPSP because the peak PP-evoked PSP evoked with inhibition intact is extremely small (<1 mV), and thus fails to evoke CA1 action potential output (as evidenced by the failure of SLM stimulation to evoke a detectable population spike in the CA1 PN cell layer; Chevaleyre and Siegelbaum, 2010; Sun et al., 2014).

Relative strength of excitation of superficial versus deep PNs by EC input reverses along the transverse axis

Our finding that both PP and SC inputs elicit a significantly smaller PSP in deep compared to superficial PNs in CA1b was surprising given that the propensity of place cell firing, which can be driven solely by direct EC input (Nakashiba et al., 2008), is greater in deep versus superficial layers of CA1 (Mizuseki et al., 2011). However, spatially-tuned MEC inputs preferentially innervate CA1 PNs located closer to CA2 (i.e. in CA1c), whereas the non-spatially tuned LEC inputs target CA1 PNs toward subiculum (i.e. in CA1a) (Steward, 1976; Wyss, 1981; Tamamaki and Nojyo, 1995; Naber et al., 2001). Thus, we examined whether direct EC drive in deep and superficial PNs varied across the transverse axis. For these experiments, we simultaneously moved the position of our recording and stimulating electrodes across the transverse axis to maintain a constant distance from recorded PNs.

We found that superficial and deep PNs in CA1a (Figure 5A), which receives direct input from LEC, showed a similar differential response to PP inputs as described above in CA1b, with nearly three-fold larger EPSPs in superficial CA1a PNs (Figure 5B). With strong (80 V) synaptic stimulation, the PP-evoked EPSP in superficial PNs was 0.94±0.16mV, whereas in deep PNs it was only 0.32±0.11mV (n=10, p<0.0001 by two-way ANOVA). There was a small but statistically significant difference in SC-evoked EPSPs in CA1a (Figure 5C), with the superficial PN EPSP (7.24±1.89 mV) slightly greater than the deep PN EPSP (6.74±1.67 mV; n=10, p=0.02 by two-way ANOVA).

When we examined the PP-evoked EPSPs in CA1c, we observed a striking reversal in the relative synaptic responses of deep versus superficial PNs compared to our CA1a and CA1b results (Figure 5D, E). In response to a strong (80 V) PP stimulus, the EPSP in deep CA1c PNs (2.31±0.55mV) was now 2.5-fold larger than the EPSP in superficial PNs (0.73±0.11mV; n=11, p<0.0001 by two-way ANOVA). SC EPSPs again were similar in amplitude in the two CA1 sublayers, although the deep PN EPSP was slightly greater at low stimulation ranges and at peak stimulation the superficial PN EPSP was slightly larger (Figure 5F: at 25V, sPN: 10.17±1.92mV, dPN: 9.0±1.53mV, n=11, p=0.038 by two-way ANOVA).

Next we determined whether PP inputs also preferentially excited deep versus superficial CA1c PNs when inhibition was intact. In the absence of GABA blockers (Figure 5G), PP-evoked PSPs in deep PNs were 3.5-fold larger than those in superficial PNs, even greater than the 2.5-fold difference in EPSP size (Figure 5H). With a strong (80 V) stimulus, the sPN PSP was 0.16±0.10mV whereas the dPN PSP was 0.53±0.15mV (n=7; p<0.0001 by two-way ANOVA). In this same cohort, we asked whether there was also a difference in the net SC-evoked PSP in deep versus superficial CA1c PNs. In contrast to the CA1c SC EPSP, the CA1c SC PSP (evoked by a 25 V stimulus) was significantly larger in superficial PNs (9.07±2.64 mV) compared to deep PNs (3.05±0.79 mV, n=7 each, p<0.0001 by two-way ANOVA; Figure 5I), similar to our CA1b results and consistent with greater inhibition of deep-layer PNs (Figure 3E).

Relative spine density in SLM dendrites of superficial and deep neurons reverses along the transverse axis

As we established above that the larger PP-evoked EPSP in CA1b superficial versus deep PNs was likely due to increased PP inputs, as judged by the relative number of SLM spines, we next asked whether the superficial/deep SLM spine density ratio also reverses across the transverse axis (Figure 6A). Similar to our CA1b results, SLM dendrite spine densities in CA1a were two-fold larger in superficial compared to deep PNs, consistent with the differences in PP-evoked EPSPs (Figure 6B left panels, 6C). Thus the spine density in CA1a superficial PNs was 1.10±0.05 spines/μm (494 spines counted on n=42 dendritic segments of average length 11±1μm, from 4 neurons) compared to 0.53±0.04 spines/μm for deep PNs (260 spines counted on n=37 dendritic segments of average length 15±1μm, from 4 neurons, p<0.0001, total from 5 animals, 8 slices). In striking contrast to our results in CA1a and CA1b, relative spine densities in deep and superficial PNs were reversed in CA1c (Figure 6B right panels, 6D), consistent with the reversed PP-evoked EPSP. Superficial PN spine density was 0.51±0.04 spines/μm (288 spines counted on n=34 dendritic segments of average length 16±1μm, from 4 neurons), approximately half the deep PN density of 0.92±0.05 spines/μm (514 spines counted on n=38 dendritic segments of average length 15±1μm, from 4 neurons, p<0.0001, total from 5 animals, 8 slices).

In contrast, in the same cells, SR dendrite spine densities in deep and superficial PNs were similar across the transverse axis, consistent with the relative constancy of the SC-evoked EPSP (Figure 6E, F; see examples in Figure S3). The SR spine density for CA1a sPNs was 1.65±0.06 spines/μm (606 spines counted on n=18 dendritic segments of average length 21±1μm) and was 1.47±0.09 spines/μm in deep PNs (444 spines counted on n=17 dendritic segments of average length 18±1μm, p=0.11). These did not differ significantly from each other or from SR spine densities for CA1c superficial PNs (1.69±0.08 spines/μm, 438 spines counted on n=12 dendritic segments of average length 22±1μm) and deep PNs (1.58±0.08 spines/μm, 389 spines counted on n=12 dendritic segments of average length 20±1μm, p=0.38).

Preferential excitation of CA1a superficial PNs by LEC and of CA1c deep PNs by MEC

Based on anatomical evidence that LEC preferentially innervates CA1a whereas MEC targets CA1c, we asked whether the reversal of the differential PP excitation of deep versus superficial PNs across the transverse axis was because LEC axons preferentially target superficial PNs and MEC axons preferentially target deep PNs. As our electrical stimulation experiments excited these axons nonspecifically, we characterized LEC and MEC responses directly using an optogenetic strategy in which we injected a viral vector (AAV2/9) expressing ChR2-EYFP under control of the CaMKII promoter into either LEC or MEC. This also had the advantage of distinguishing EC inputs versus excitatory inputs from nucleus reuniens, whose axons also course through SLM to target CA1 PN SLM dendrites (Wouterlood et al., 1990; Dolleman-Van der Weel and Witter, 1996). After two to three weeks, there was robust infection of LEC or MEC axons in CA1 that could be visualized in SLM by immunohistochemical staining for EYFP (Figure 7A, D).

We prepared acute dorsal hippocampal slices from injected mice and, with inhibition blocked, used LED illumination to excite LEC or MEC axons while recording the light-evoked EPSPs from deep and superficial PNs of CA1a and CA1c in a single slice. EPSPs were normalized by the amplitude of best responder neuron in the slice. A comparison of normalized EPSPs in single slices allowed us to determine the relative synaptic drive evoked by a given EC input in deep versus superficial PNs in CA1a compared to CA1c. The within-slice comparison was chosen to minimize the effect of variability caused by differential levels of viral expression among individual slices or different animals. Normalized stimulus-response input-output curves were generated by measuring EPSPs from the four classes of neurons in response to varying LED power.

As predicted from the pattern of EC innervation and our electrical stimulation results, photostimulation of LEC axons (Figure 7B, C) elicited the largest EPSP in CA1a superficial PNs, which was approximately two-fold larger than the EPSP in CA1a deep PNs (at 100% power, the CA1a dPN EPSP was 45.4±7.1% the size of the CA1a sPN). However, CA1a responses were much larger than CA1c responses. There was a statistically significant difference in LEC-evoked input-output curves among the four PN subtypes (n=8 for CA1a sPN, 6 for CA1a dPN, 7 for CA1c sPN, 7 for CA1c dPN, from 6 slices and 6 mice; $p<0.0001$ by ANOVA, $p<0.05$ between all pairs by Tukey's multiple comparisons test). At 100% power, the CA1c deep PN EPSP was 21.6±7.4% and the CA1c superficial PN EPSP was 3.9±2.0% the size of the CA1a superficial PN EPSP. Non-normalized EPSP voltage-response curves yielded qualitatively similar differences (Figure S4A).

In contrast to our LEC findings, photostimulation of MEC inputs (Figure 7E, F) evoked the largest EPSP in CA1c deep PNs, which was approximately 2.5-fold larger than the EPSP in CA1c superficial PNs. At 100% power, the CA1c superficial PN EPSP was 41.4±6.4% the amplitude of the CA1c deep PN EPSP. As with LEC activation, there were statistically significant differences in MEC-evoked EPSPs among the four PN subtypes (n=6 each, from 6 slices and 5 mice, $p<0.0001$ by ANOVA, $p<0.05$ between all pairs by Tukey's multiple comparisons test). Consistent with anatomical findings, photostimulation of MEC axons evoked much smaller EPSPs in CA1a versus CA1c PNs. At 100% power, the CA1a superficial PN EPSP was 18.8±4.5% and the CA1a deep PN EPSP was 4.9±4.2% of the CA1c deep PN EPSP. Again, non-normalized EPSP curves yielded similar results (Figure S4B).

These results provide functional evidence that LEC preferentially excites CA1a PNs whereas MEC preferentially excites CA1c PNs, in accord with anatomical results (Steward, 1976; Wyss, 1981; Tamamaki and Nojyo, 1995; Naber et al., 2001). Moreover, our findings suggest that LEC and MEC axons within a given subregion show a similar preference for deep versus superficial neurons. Finally, radial sublayer preference appears to be largely a function of the relative number of SLM dendritic spines on deep versus superficial PNs that are available to the inputs in each transverse subregion.

DISCUSSION

Previous studies found that CA1 PNs form two functionally distinct sublayers along the radial axis. These superficial and deep sublayers differ in their developmental time course, expression of molecular markers, local inhibitory circuitry, and modulation by neurotransmitters (Bayer, 1980; Dong et al., 2009; Lee et al., 2014; Valero et al., 2015; Cembrowski et al., 2016; Maroso et al., 2016). Our study extends this by revealing that functionally distinct areas of EC provide direct excitatory input that differentially engages the two radial sublayers. Importantly, the relative weight of EC excitation of deep versus superficial PNs varies according to the transverse axis position of the CA1 PN. Thus, near the subiculum border (CA1a), EC delivers stronger excitation to superficial compared to deep PNs. Strikingly, this differential drive is reversed in CA1 PNs near the CA2 border (CA1c), where EC provides a much stronger synaptic drive to deep versus superficial PNs. In contrast to the marked differences in EC input, Schaffer collaterals of CA3 neurons provide relatively constant excitatory drive across the CA1 radial and transverse axes, but with much greater feedforward inhibition of deep compared to superficial PNs across the transverse axis. In contrast, EC inputs evoked a similar extent of feedforward inhibition of deep and superficial PNs across the transverse axis.

What is the mechanism for this differential cortical drive and what controls the variation of MEC versus LEC excitatory influence along the transverse axis? Classical anatomical studies demonstrated that medial entorhinal cortex (MEC) and lateral entorhinal cortex (LEC) axons target different regions of CA1 along its transverse axis, with MEC preferentially targeting CA1 toward CA2 (CA1c) and LEC preferentially targeting CA1 towards subiculum (CA1a) (Steward, 1976; Wyss, 1981; Tamamaki and Nojyo, 1995; Naber et al., 2001). We provide physiological evidence confirming these anatomical findings by showing that MEC axons preferentially excite CA1c PNs whereas LEC axons preferentially excite CA1a PNs.

The finding that CA1a superficial PNs are most strongly driven by LEC whereas CA1c deep PNs are most strongly driven by MEC suggested that MEC axons preferentially form synapses with deep PNs whereas LEC axons preferentially form synapses with superficial PNs. Alternatively, LEC and MEC inputs may not distinguish between radial sublayers; rather, synaptic strength may simply be determined by SLM spine number in a given class of neurons and the local density of input fibers. Our results favor the latter (Figure 7G) as LEC and MEC inputs elicit larger EPSPs in superficial relative to deep PNs in CA1a, reflecting the greater number of SLM spines in superficial PNs, whereas the same two inputs both elicit larger EPSPs in deep compared to superficial PNs in CA1c, again reflecting the relative difference in SLM spines. The signals that determine radial and transverse variations in spine density remain unknown.

Does the variation in EC drive represent a sharp distinction or a gradient along the two axes? In our experiments, we mostly targeted neurons located at the extremes of the CA1 radial axis, and therefore cannot determine whether neurons in the middle of SP show intermediate responses to EC input. The similarity between the properties of CA1b and CA1a PNs possibly suggest a relatively steep gradient between CA1b and CA1c. However, our CA1b recordings were from mid-CA1b to the CA1a border. Thus, there may be a more gradual gradient from mid-CA1b to CA1c. In vivo evidence suggests that there may be a graded transition along both axes. Place cell propensity increases steadily from superficial to middle to deep CA1 PNs (Mizuseki et al., 2011) and spatial information gradually increases from CA1a to CA1c (Henriksen et al., 2010). A gradient in connectivity would be in line with evidence that gene expression (Cembrowski et al., 2016) and intrinsic excitability (Jarsky et al., 2008; Malik et al., 2016) also evolve across anatomical axes.

Putative influence of differential cortical drive on single neuron dynamics

Multiple studies suggest that direct EC inputs to CA1 may play important roles in regulating CA1 activity and hippocampal dependent learning and memory. How might the two- to three-fold difference in perforant pathway EPSP size between superficial and deep PNs influence CA1 activity? Despite their large voltage attenuation at the soma (Golding et al., 2005), EC EPSPs can sum at high frequencies to trigger local Ca^{2+} spikes, producing large Ca^{2+} transients in the SLM dendrites of CA1 PNs (Tsay et al., 2007) that can induce local long-term synaptic potentiation (Golding et al., 2002; Nolan et al., 2004; Remondes and Schuman, 2002; Ahmed and Siegelbaum 2009). It is thus possible that levels of Ca^{2+} amplification and EC input plasticity differ along the radial axis. Additionally, direct EC inputs can also influence SC synaptic strength via a form of heterosynaptic plasticity termed input-timing-dependent plasticity or ITDP (Dudman et al., 2007; Basu et al., 2013) that can enhance the precision of contextual memory (Basu et al., 2016). Finally, brief trains of EC inputs can interact with SC inputs to generate plateau potentials that modulate location-dependent place cell firing *in vivo* (Bittner et al., 2015). Our findings suggest that such processes are likely to be recruited to a variable degree along the radial and transverse axes. For example, in CA1a, ITDP may be more readily induced in superficial versus deep PNs because of stronger EC drive and their predominant perisomatic inhibition by CCK interneurons (Valero et al., 2015) that contribute strongly to ITDP expression (Basu et al., 2013).

Consequences of differential cortical drive on CA1 responses to behavior

Previous work by Mizuseki et al. (2011) showed that place cells are more likely to be found in the deep CA1 pyramidal layer, although the recording location along the transverse axis was not specified. Our results provide a potential circuit mechanism for this finding, at least in CA1c, an area with the highest degree of spatial tuning (Henriksen et al., 2010) and where we find that direct excitatory drive from the superficial layers of MEC is significantly stronger to deep versus superficial PNs.

In CA1a, place cells have been reported with similar frequency as in CA1c (radial sublayer unidentified) but with a greater number of place fields and reduced phase-locked firing with MEC theta rhythms, indicating less spatial specificity (Henriksen et al., 2010). It is unclear whether CA1a place cell activity is mediated by the weak MEC input with strong spatial content, strong LEC input with weak spatial content (Hargreaves et al., 2005), or is more dependent on Schaffer collateral input. This last option is possible given that SC input to CA1a largely derives from the CA3 subregion (CA3c, near dentate gyrus) with the highest degree of spatial tuning (Ishizuka et al., 1990; Lu et al., 2015). In CA1a, we find that MEC drive is weak but favors superficial PNs, as does the strong LEC input, and net SC excitation. Therefore, CA1a superficial PNs may be more likely to have location-dependent firing. Future studies in which deep and superficial place cell activity is assessed across the transverse axis would help answer these questions.

Might our results help explain the responses of CA1 PNs in non-spatial behaviors or the modulation of their location-dependent firing by non-spatial stimuli? CA1a neurons respond to objects with an increase in place cell number and average number of place fields per cell, hypothesized to reflect preferential LEC innervation of this area (Burke et al., 2011). However, many units did not display such modulation. Similarly, during an olfactory associative task many, but not all, CA1a and LEC units showed increasing phase locking at 20–40 Hz that correlated with task performance and odor selective responses (Igarashi et al., 2014). Our findings suggest that weakly modulated units may correspond to deep PNs, receiving weak LEC drive, whereas heavily modulated units may represent superficial PNs, strongly driven by LEC. A role for differential SC input is also possible, given increased net SC excitation to superficial PNs and the finding that CA1a is innervated by CA3c (close to dentate gyrus), which shows higher *Arc* expression after a non-spatial recognition memory task than do other regions of CA3 (Nakamura et al., 2013).

Effect of differential cortical drive of CA1 subpopulations on network dynamics

What function might the distinct CA1 radial sublayers serve? In addition to EC input differences we have described, the two layers are differentially driven by CA2 (Kohara et al., 2014), which provides stronger excitation to deep PNs (although transverse axis variation is unknown). In addition, superficial PNs can produce strong feedforward inhibition of deep PNs (Lee et al., 2014). Thus, the two layers may act as parallel circuits, with superficial PNs in CA1a and CA1b preferentially tuned to EC and CA3 input, and deep PNs tuned to CA3 and CA2 inputs and inhibited by superficial CA1 PNs. In both sublayers, CA3 is likely to provide the strongest excitatory drive, with EC and CA2 inputs exerting a more modulatory control.

In addition to differences in extrinsic inputs, the sublayers also have distinct intrinsic properties that may contribute to their different functions. Superficial and deep PNs express distinct proteins, such as calbindin, zinc, and kinases, which may differentially influence intracellular calcium handling and plasticity (Slomianka et al., 2011; Maroso et al., 2016). For example, a recent study demonstrated that superficial PNs, and not deep PNs, possess an intracellular pathway coupled to the CB1 receptor that allows for endocannabinoid modulation of HCN channel function and, in turn, LTP of SC inputs (Maroso et al., 2016).

Finally, deep and superficial CA1 PNs project to diverse areas that may dictate the dynamics and information content appropriate to different behavioral outputs. For example, in ventral hippocampus, superficial PNs primarily project to entorhinal cortex whereas deep PNs also project to amygdala, prefrontal cortex, olfactory cortices, and other subcortical structures (Arszovski et al., 2014; Lee et al., 2014; Ciocchi et al., 2015). Indeed, a recent study suggests that projections from deep layer ventral CA1 to nucleus accumbens are critical for social memory (Okuyama et al., 2016). Furthermore, the targeting of perisomatic CCK+ interneuron-mediated inhibition to superficial PNs and PV+ interneuron-mediated inhibition to deep PNs, as well as the potential of superficial-to-deep feedforward inhibition (Lee et al., 2014; Valero et al., 2015), could establish temporal dynamics and plasticity mechanisms that may help implement different behaviors mediated by EC inputs (Freund, 2003; Armstrong and Soltesz, 2011; Stark et al., 2014; Ciocchi et al., 2015; Valero et al., 2015). Exploration of these questions awaits further methodological tools to enable the selective manipulation of CA1 PN subpopulations.

EXPERIMENTAL PROCEDURES

All experiments were performed according to National Institutes of Health guidelines and with approval from the Columbia University Institutional Animal Care and Use Committee.

Animals

Experiments were conducted on male C57/BL6 mice (Jackson Labs) aged 6–8 weeks.

Solutions

Recording artificial cerebrospinal fluid (rACSF) was composed of NaCl (125mM), $NaHCO_3$ (25mM), KCl (2.5mM), NaH_2PO_4 (1.25mM), $MgCl_2$ (1mM), $CaCl_2$ (2mM), D-glucose (22.5mM), Na-pyruvate (3mM), L-ascorbic acid (1mM). Dissection artificial cerebrospinal fluid (dACSF) was composed of NaCl (10mM), $NaHCO_3$ (25mM), KCl (2.5mM), NaH_2PO_4 (1.25mM), $MgCl_2$ (7mM), $CaCl_2$ (0.5mM), sucrose (195mM), D-glucose (10mM), Na-pyruvate (2mM). ACSF pH was approximately 7.3 after oxygenation with 95%/5% O_2/CO_2. Intracellular solution contained $KMeSO_3$ (135mM), KCl (5mM), NaCl (2mM), EGTA (0.2mM), HEPES (10mM), Na_2phosphocreatine (10mM), MgATP (5mM), Na_2GTP (0.4mM), pH adjusted to 7.3. For morphological analysis, 0.2% biocytin hydrazide (Invitrogen) was added to the intracellular solution, with pH readjusted. For two-photon imaging, 25μM Alexa Fluor 594 was also added. Pharmacology was performed via bath application of the following, obtained from either Sigma or Tocris: SR95531, CGP55845, D-APV, and CNQX.

Viruses and Surgery

Optogenetic activation of LEC and MEC axons was achieved by stereotaxic injection of a non-Cre-dependent adeno-associated virus (AAV 2/9) expressing ChR2. The virus, pAAV-CaMKIIa-hChR2(H134R)-EYFP, was a gift from Karl Deisseroth (Addgene plasmid #26969, prepared by UNC Vector Core). For stereotaxic surgery, mice were anesthetized with continuous isofluorane delivery. Temperature and anesthesia depth were periodically monitored. Injections were of 180nl, made bilaterally to either LEC or MEC. Coordinates relative to bregma were (AP −3.2, ML ±4.6, DV −3.6) for LEC and (AP −4.7, ML ±3.3, DV −3.3) for MEC. Mice recovered for two to three weeks to allow for adequate viral expression in the terminals. Slices were then prepared as below.

Slice Preparation and Electrophysiology

Mice were anesthetized with isofluorane and underwent intracardiac perfusion with chilled, oxygenated dACSF. After decapitation, brains were removed and hippocampi were dissected in chilled, oxygenated dACSF. Once isolated hippocampi were mounted in elongated fashion on a 4% agar block, transverse 400-μm sections were made beginning at the dorsal aspect using a Leica VT1200S vibratome, while maintaining dACSF temperature below 5°C. The first two to three slices bilaterally were discarded and the next six bilaterally, consisting of dorsal hippocampus, were transferred to an incubation chamber containing a continuously oxygenated mixture of 50% dACSF and 50% rACSF at 34°C. After approximately 25 minutes, slices were kept in this chamber at 20–25°C until use in experiments.

Electrophysiology was conducted in continuously oxygenated rACSF maintained at 34°C. Whole-cell recordings were obtained using fire-polished borosilicate glass pipettes (Sutter) pulled to tip resistances of 3.8–5.0 MΩ. CA1 PNs were visually targeted in stratum pyramidale (SP) using infrared (IR) differential interference contrast imaging with an Olympus OLY-150 IR CCD camera and a 60x, 0.9NA water immersion objective (Olympus). Superficial CA1 PN somata were defined as the first row of PNs at the border of SP and stratum radiatum (SR). Superficial CA1 PN somata were approached approximately within 10μm from the SP-SR border, whereas deep CA1 PN somata were approached approximately 10μm from the SP-SO border. Superficial and deep PNs were generally recorded in alternating fashion. For experiments in CA1a and CA1c, superficial and deep PNs were recorded in the same slice and at the same transverse position. For optogenetic experiments, neurons were targeted in the same slice and the order of the four neurons (CA1a vs. CA1c, superficial vs. deep) was varied. Recordings were performed with the Multiclamp 700B amplifier and pClamp 9 software (Axon Instruments), with data digitized by the Digidata 1322A system. Data were acquired at 20kHz with 10-kHz Bessel low-pass filtering applied via the amplifier. Gigaseal and break-in were achieved in voltage clamp mode, and measurements made in current clamp mode, waiting at least five minutes after break-in and membrane potential held at −70 mV. PN identity was confirmed in current clamp by an accommodating firing pattern to positive current injection and large voltage sag at hyperpolarized potentials with negative current injections. Series resistance was compensated in current clamp mode using the bridge balance and was measured periodically during the experiments. Recordings were continued if series resistance was maintained below 25 MΩ.

Extracellular electrical stimulation of SR and SLM axons was achieved by using a constant voltage isolator (Digitimer Ltd) to deliver voltage to low resistance (500–750kΩ), rACSF-filled glass pipettes placed in each stratum. Pulses were 0.1 ms in duration and given every 30 seconds for SC or PP stimuli. Extracellular stimulation voltage range was 10–80V for SLM stimulation, as this gave consistent subthreshold voltage responses typical for PP synaptic potentials. Voltage range was 2.5–25V for SRstimulation, as this elicited consistent subthreshold voltage responses typical for SC responses; above this range, in some neurons, larger responses led to action potentials in the absence of inhibition. For experiments with inhibition blocked, a cut was made beforehand at CA3/CA2 to prevent epileptic activity.

Light Delivery

For optogenetic experiments, light was delivered from a 470-nm collimated blue LED (Thorlabs) that was back mounted. Light was focused through the objective (Olympus, 60x, 0.9 NA) onto the slice with full-field illumination. Photostimulation pulses were 2 ms in duration and intensity was varied from 10 to 100% max light intensity, averaging 3–5 trials per point. Stimulation was done once every 30 s.

Morphological Analysis

Neurons were filled with biocytin via whole cell recording for 10–15 minutes. Slices were fixed in 4% paraformaldehyde (PFA) in 1x phosphate buffered saline (PBS). Morphology was revealed with the avidin-biotinylated horseradish peroxidase complex reaction (Vectastain ABC Kit, Vector Laboratories) or by fluorescent immunohistochemistry of biocytin (see below). Tracing and dendritic length measurements were performed using Neurolucida (Version 8, MBF Bioscience), with no significant differences in length measurement between the two methods.

Immunohistochemistry and Imaging

After recording, slices were fixed overnight in 4% PFA in PBS. Slices were washed in PBS, then permeabilized and blocked (0.4% Triton X-100 and 5% Normal goat serum in PBS). ChR2-EYFP projections were stained overnight at 4°C with rabbit polyclonal anti-GFP primary antibody (1:1000 dilution; A-11122, ThermoFisher) in blocking solution (0.2% Triton X-100 and 5% NGS in PBS). Sections were washed 3 × 15 min in PBS the following day and incubated for 2 h at room temperature with goat anti-rabbit Alexa Fluor 488 secondary antibody (1:500 dilution; A-11008, ThermoFisher) in blocking solution. Recorded neurons filled with 0.2% biocytin were stained with streptavidin-bound Alexa Fluor 647 conjugate (1:500 dilution; S32357, ThermoFisher) for 2 h at room temperature in PBS. Nuclei were stained with Hoescht (1:1000 dilution; H3570, ThermoFisher) for 10 min at room temperature in PBS. Slices were washed 3 × 15 min in PBS, mounted in Fluoromount (F4680, Sigma), and imaged on an inverted laser scanning confocal microscope (LSM 700, Zeiss). For neuronal morphology, confocal z-stacks were obtained with 1.5μm thick optical sections.

Two-photon imaging

Spine imaging was performed with a Prairie Technologies Ultima two-photon microscope. Whole cell recordings from CA1 PNs were achieved as above and filled via the patch pipette with 25 μm Alexa Fluor 594, allowing at least 35 minutes for dye to reach SLM tuft dendrites. We examined one PN per slice to avoid ambiguity of the source of the dendritic processes. To avoid biased sampling, imaging was performed by an individual, separate from the electrophysiologist, who was blinded to neuronal location. Dye was excited at 820 nm. SR spines were examined in oblique secondary branches of the primary apical dendrite, avoiding SLM and SR borders. SLM spines were examined in tuft dendrites after the bifurcation of the primary apical dendrite, greater than 350 μm from the soma. Analysis focused on medium and thin diameter SLM branches versus thicker branches at the SR-SLM border (Megias et al., 2001). For each area, multiple dendritic branches and branch segments were imaged, avoiding terminal ends and branch points. Spines were counted by an observer blinded to neuronal location. Density for a particular segment was calculated by dividing spine number by segment length. Total spine number was calculated by multiplying the average spine densities by dendritic lengths measured by biocytin labeling above. Biocytin labeling with Neurolucida reconstruction achieved better resolution and assessment of architecture than two-photon laser scanning microscopy. However, yield was lower and thus a separate group of PNs was used for length measurement versus spine counting.

Data Analysis

Clampfit was used for the analysis of electrophysiological data. ImageJ was used for image processing and spine counting. Prism (Graphpad) was used for statistical analysis. Statistical errors shown are standard errors of the mean. Significance was computed using two-way ANOVA to compare response curves and unpaired t-tests for spines and morphological data.

Supplementary Material

Refer to Web version on PubMed Central for supplementary material.

Acknowledgments

We would like to thank Sami Hassan for assistance with artwork. This work was supported by NIH T32MH020004 (A.V.M.), the Charles and Lee Brown Fellowship (A.V.M.), the Columbia University Amgen Scholars Summer Research Program (D.C.L.), NIH R01NS036658 (S.A.S.) and the Howard Hughes Medical Institute (S.A.S.).

References

Bannister NJ, Larkman AU. Dendritic morphology of CA1 pyramidal neurones from the rat hippocampus: I. Branching patterns. J Comp Neurol. 1995; 360:150–160. [PubMed: 7499560]

Basu J, Srinivas KV, Cheung SK, Taniguchi H, Huang ZJ, Siegelbaum SA. A cortico-hippocampal learning rule shapes inhibitory microcircuit activity to enhance hippocampal information flow. Neuron. 2013; 79:1208–1221. [PubMed: 24050406]

Basu J, Zaremba JD, Cheung SK, Hitti FL, Zemelman BV, Losonczy A, Siegelbaum SA. Gating of hippocampal activity, plasticity, and memory by entorhinal cortex long-range inhibition. Science. 2016; 351:aaa5694. [PubMed: 26744409]

Bittner KC, Grienberger C, Vaidya SP, Milstein AD, Macklin JJ, Suh J, Tonegawa S, Magee JC. Conjunctive input processing drives feature selectivity in hippocampal CA1 neurons. Nat Neurosci. 2015; 18:1133–1142. [PubMed: 26167906]

Burke SN, Maurer AP, Nematollahi S, Uprety AR, Wallace JL, Barnes CA. The influence of objects on place field expression and size in distal hippocampal CA1. Hippocampus. 2011; 21:783–801. [PubMed: 21365714]

Brun VH, Leutgeb S, Wu HQ, Schwarcz R, Witter MP, Moser EI, Moser MB. Impaired spatial representation in CA1 after lesion of direct input from entorhinal cortex. Neuron. 2008; 57:290–302. [PubMed: 18215625]

Cembrowski MS, Bachman JL, Wang L, Sugino K, Shields BC, Spruston N. Spatial Gene-Expression Gradients Underlie Prominent Heterogeneity of CA1 Pyramidal Neurons. Neuron. 2016; 89:351–368. [PubMed: 26777276]

Chevaleyre V, Siegelbaum SA. Strong CA2 pyramidal neuron synapses define a powerful disynaptic cortico-hippocampal loop. Neuron. 2010; 66:560–572. [PubMed: 20510860]

Ciocchi S, Passecker J, Malagon-Vina H, Mikus N, Klausberger T. Brain computation. Selective information routing by ventral hippocampal CA1 projection neurons. Science. 2015; 348:560–563. [PubMed: 25931556]

Deshmukh SS, Knierim JJ. Representation of non-spatial and spatial information in the lateral entorhinal cortex. Front Behav Neurosci. 2011; 5:69. [PubMed: 22065409]

Dolleman-Van Der Weel MJ, Witter MP. Projections from the nucleus reuniens thalami to the entorhinal cortex, hippocampal field CA1, and the subiculum in the rat arise from different populations of neurons. J Comp Neurol. 1996; 364:637–650. [PubMed: 8821451]

Dong HW, Swanson LW, Chen L, Fanselow MS, Toga AW. Genomic-anatomic evidence for distinct functional domains in hippocampal field CA1. Proc Natl Acad Sci U S A. 2009; 106:11794–11799. [PubMed: 19561297]

Dougherty KA, Islam T, Johnston D. Intrinsic excitability of CA1 pyramidal neurones from the rat dorsal and ventral hippocampus. J Physiol. 2012; 590:5707–5722. [PubMed: 22988138]

Dudman JT, Tsay D, Siegelbaum SA. A role for synaptic inputs at distal dendrites: instructive signals for hippocampal long-term plasticity. Neuron. 2007; 56:866–879. [PubMed: 18054862]

Freund TF. Interneuron Diversity series: Rhythm and mood in perisomatic inhibition. Trends Neurosci. 2003; 26:489–495. [PubMed: 12948660]

Freund TF. Interneuron Diversity series: Rhythm and mood in perisomatic inhibition. Trends Neurosci. 2003; 26:489–495. [PubMed: 12948660]

Fyhn M, Molden S, Witter MP, Moser EI, Moser MB. Spatial representation in the entorhinal cortex. Science. 2004; 305:1258–1264. [PubMed: 15333832]

Golding NL, Kath WL, Spruston N. Dichotomy of action-potential backpropagation in CA1 pyramidal neuron dendrites. J Neurophysiol. 2001; 86:2998–3010. [PubMed: 11731556]

Golding NL, Mickus TJ, Katz Y, Kath WL, Spruston N. Factors mediating powerful voltage attenuation along CA1 pyramidal neuron dendrites. J Physiol. 2005; 568:69–82. [PubMed: 16002454]

Golding NL, Staff NP, Spruston N. Dendritic spikes as a mechanism for cooperative long-term potentiation. Nature. 2002; 418:326–331. [PubMed: 12124625]

Graves AR, Moore SJ, Bloss EB, Mensh BD, Kath WL, Spruston N. Hippocampal pyramidal neurons comprise two distinct cell types that are countermodulated by metabotropic receptors. Neuron. 2012; 76:776–789. [PubMed: 23177962]

Hargreaves EL, Rao G, Lee I, Knierim JJ. Major dissociation between medial and lateral entorhinal input to dorsal hippocampus. Science. 2005; 308:1792–1794. [PubMed: 15961670]

Hartzell AL, Burke SN, Hoang LT, Lister JP, Rodriguez CN, Barnes CA. Transcription of the immediate-early gene Arc in CA1 of the hippocampus reveals activity differences along the proximodistal axis that are attenuated by advanced age. J Neurosci. 2013; 33:3424–3433. [PubMed: 23426670]

Henriksen EJ, Colgin LL, Barnes CA, Witter MP, Moser MB, Moser EI. Spatial representation along the proximodistal axis of CA1. Neuron. 2010; 68:127–137. [PubMed: 20920796]

Igarashi KM, Lu L, Colgin LL, Moser MB, Moser EI. Coordination of entorhinal-hippocampal ensemble activity during associative learning. Nature. 2014; 510:143–147. [PubMed: 24739966]

Ishizuka N, Weber J, Amaral DG. Organization of intrahippocampal projections originating from CA3 pyramidal cells in the rat. J Comp Neurol. 1990; 295:580–623. [PubMed: 2358523]

Ito HT, Schuman EM. Functional division of hippocampal area CA1 via modulatory gating of entorhinal cortical inputs. Hippocampus. 2012; 22:372–387. [PubMed: 21240920]

Jarsky T, Mady R, Kennedy B, Spruston N. Distribution of bursting neurons in the CA1 region and the subiculum of the rat hippocampus. J Comp Neurol. 2008; 506:535–547. [PubMed: 18067146]

Kitamura T, Pignatelli M, Suh J, Kohara K, Yoshiki A, Abe K, Tonegawa S. Island cells control temporal association memory. Science. 2014; 343:896–901. [PubMed: 24457215]

Kohara K, Pignatelli M, Rivest AJ, Jung HY, Kitamura T, Suh J, Frank D, Kajikawa K, Mise N, Obata Y, et al. Cell type-specific genetic and optogenetic tools reveal hippocampal CA2 circuits. Nat Neurosci. 2014; 17:269–279. [PubMed: 24336151]

Lee SH, Marchionni I, Bezaire M, Varga C, Danielson N, Lovett-Barron M, Losonczy A, Soltesz I. Parvalbumin-positive basket cells differentiate among hippocampal pyramidal cells. Neuron. 2014; 82:1129–1144. [PubMed: 24836505]

Lorente de Nó R. Studies on the structure of the cerebral cortex. II. Continuation of the study of the ammonic system. J Psychol Neurol. 1934; 46:113–177.

Lu L, Igarashi KM, Witter MP, Moser EI, Moser MB. Topography of Place Maps along the CA3-to-CA2 Axis of the Hippocampus. Neuron. 2015; 87:1078–1092. [PubMed: 26298277]

Malik R, Dougherty KA, Parikh K, Byrne C, Johnston D. Mapping the electrophysiological and morphological properties of CA1 pyramidal neurons along the longitudinal hippocampal axis. Hippocampus. 2016; 26:341–361. [PubMed: 26333017]

Maroso M, Szabo GG, Kim HK, Alexander A, Bui AD, Lee SH, Lutz B, Soltesz I. Cannabinoid Control of Learning and Memory through HCN Channels. Neuron. 2016; 89:1059–1073. [PubMed: 26898775]

Megias M, Emri Z, Freund TF, Gulyas AI. Total number and distribution of inhibitory and excitatory synapses on hippocampal CA1 pyramidal cells. Neuroscience. 2001; 102:527–540. [PubMed: 11226691]

Mizuseki K, Diba K, Pastalkova E, Buzsaki G. Hippocampal CA1 pyramidal cells form functionally distinct sublayers. Nat Neurosci. 2011; 14:1174–1181. [PubMed: 21822270]

Naber PA, Lopes da Silva FH, Witter MP. Reciprocal connections between the entorhinal cortex and hippocampal fields CA1 and the subiculum are in register with the projections from CA1 to the subiculum. Hippocampus. 2001; 11:99–104. [PubMed: 11345131]

Nakamura NH, Flasbeck V, Maingret N, Kitsukawa T, Sauvage MM. Proximodistal segregation of nonspatial information in CA3: preferential recruitment of a proximal CA3-distal CA1 network in nonspatial recognition memory. J Neurosci. 2013; 33:11506–11514. [PubMed: 23843521]

Nakashiba T, Young JZ, McHugh TJ, Buhl DL, Tonegawa S. Transgenic inhibition of synaptic transmission reveals role of CA3 output in hippocampal learning. Science. 2008; 319:1260–1264. [PubMed: 18218862]

Okuyama T, Kitamura T, Roy DS, Itohara S, Tonegawa S. Ventral CA1 neurons store social memory. Science. 2016; 353:1536–1541. [PubMed: 27708103]

Remondes M, Schuman EM. Direct cortical input modulates plasticity and spiking in CA1 pyramidal neurons. Nature. 2002; 416:736–740. [PubMed: 11961555]

Slomianka L, Amrein I, Knuesel I, Sorensen JC, Wolfer DP. Hippocampal pyramidal cells: the reemergence of cortical lamination. Brain Struct Funct. 2011; 216:301–317. [PubMed: 21597968]

Stark E, Roux L, Eichler R, Senzai Y, Royer S, Buzsaki G. Pyramidal cell-interneuron interactions underlie hippocampal ripple oscillations. Neuron. 2014; 83:467–480. [PubMed: 25033186]

Steward O. Topographic organization of the projections from the entorhinal area to the hippocampal formation of the rat. J Comp Neurol. 1976; 167:285–314. [PubMed: 1270625]

Suh J, Rivest AJ, Nakashiba T, Tominaga T, Tonegawa S. Entorhinal cortex layer III input to the hippocampus is crucial for temporal association memory. Science. 2011; 334:1415–1420. [PubMed: 22052975]

Sun Q, Srinivas KV, Sotayo A, Siegelbaum SA. Dendritic Na+ spikes enable cortical input to drive action potential output from hippocampal CA2 pyramidal neurons. Elife. 2014; 3

Tamamaki N, Nojyo Y. Preservation of topography in the connections between the subiculum, field CA1, and the entorhinal cortex in rats. J Comp Neurol. 1995; 353:379–390. [PubMed: 7538515]

Tsao A, Moser MB, Moser EI. Traces of experience in the lateral entorhinal cortex. Curr Biol. 2013; 23:399–405. [PubMed: 23434282]

Tsay D, Dudman JT, Siegelbaum SA. HCN1 channels constrain synaptically evoked Ca2+ spikes in distal dendrites of CA1 pyramidal neurons. Neuron. 2007; 56:1076–1089. [PubMed: 18093528]

Valero M, Cid E, Averkin RG, Aguilar J, Sanchez-Aguilera A, Viney TJ, Gomez-Dominguez D, Bellistri E, de la Prida LM. Determinants of different deep and superficial CA1 pyramidal cell dynamics during sharp-wave ripples. Nat Neurosci. 2015; 18:1281–1290. [PubMed: 26214372]

Wouterlood FG, Saldana E, Witter MP. Projection from the nucleus reuniens thalami to the hippocampal region: light and electron microscopic tracing study in the rat with the anterograde tracer Phaseolus vulgaris-leucoagglutinin. J Comp Neurol. 1990; 296:179–203. [PubMed: 2358531]

Wyss JM. An autoradiographic study of the efferent connections of the entorhinal cortex in the rat. J Comp Neurol. 1981; 199:495–512. [PubMed: 6168668]

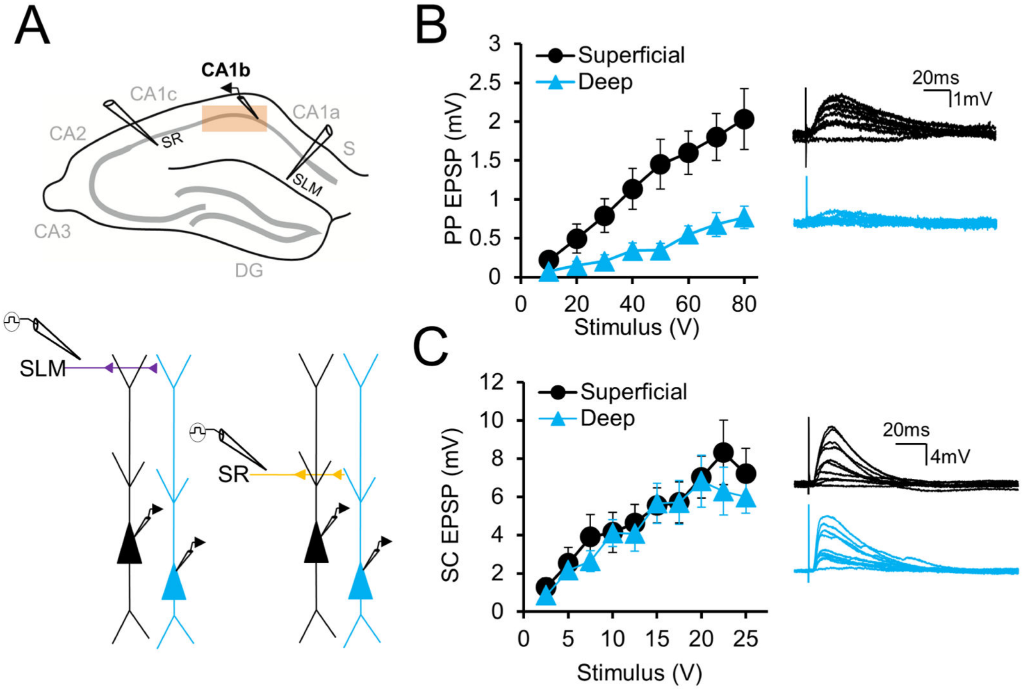

Figure 1. Larger excitatory responses to PP stimulation in superficial compared to deep CA1 PNs in CA1b

(A) CA1b area targeted (above) and experimental paradigm (below), with extracellular electrode placement in SR and SLM. (B) Left, input-output curves of perforant path EPSPs elicited in deep and superficial PNs (n = 28 each) by extracellular SLM stimulation. Right, example traces with increasing stimulation in a superficial (black) and deep (blue) PN. (C) Left, input-output curves of Schaffer collateral EPSPs elicited in deep and superficial PNs (n = 23 each) by extracellular SR stimulation. Right, example traces with increasing stimulation in a superficial (black) and deep (blue) PN. Error bars represent ±SEM.

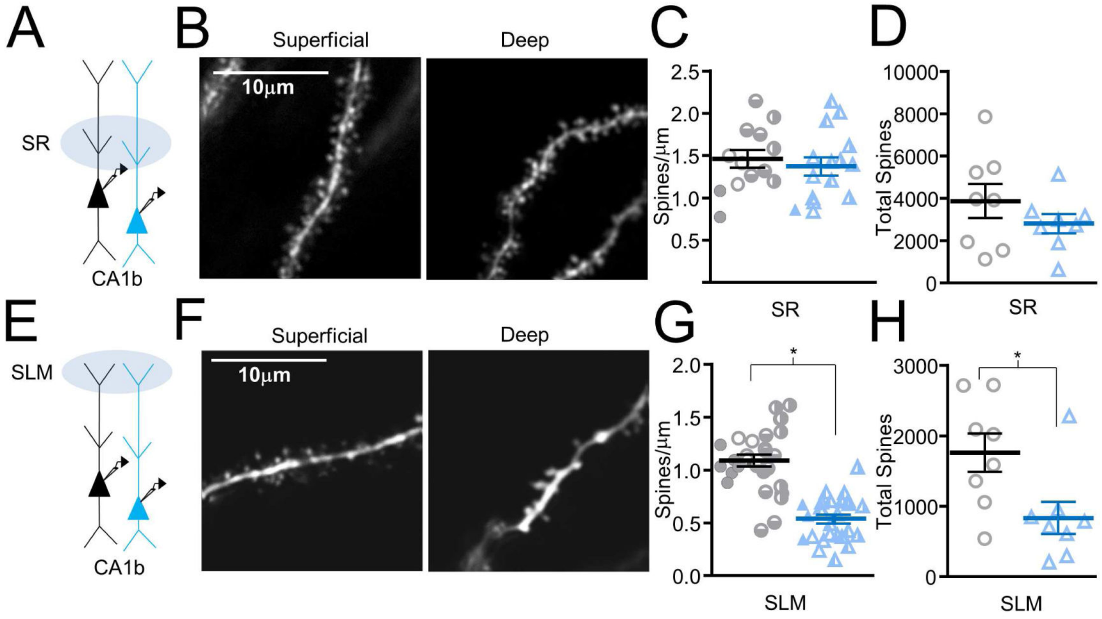

Figure 2. Increased dendrite spine density and spine number in SLM of superficial versus deep CA1 PNs in CA1b

(A) Apical dendrite region imaged for SR dendritic spine density measurement. (B) Two-photon image of an SR oblique dendrite of a superficial (left) and deep (right) CA1 PN. (C) SR spine densities (sPN: n=13 dendritic branch segments from 4 neurons; dPN: n=14 segments from 4 neurons). Symbols represent single dendritic branches, with a different symbol for each neuron. (D) Total SR spine number (based on n=8 sPN, 8 dPN). Symbols represent individual neurons. (E) Apical dendrite region imaged for SLM dendritic spine density measurement. (F) Two-photon image of an SLM dendrite of a superficial (left) and deep (right) CA1 PN. (G) SLM spine densities (sPN: n=29 dendritic branch segments from 4 neurons; dPN: n=26 segments from 4 neurons). Symbols represent single dendritic segment, with a different symbol for each neuron. (H) Total SLM spine number (based on n=8 sPN, 8 dPN). Symbols represent individual neurons. For C, D, G, H, horizontal line shows mean (sPN, black; dPN, blue) and error bars show ±SEM. Figure S1 shows dendritic lengths for individual PNs used to calculate average spine numbers.

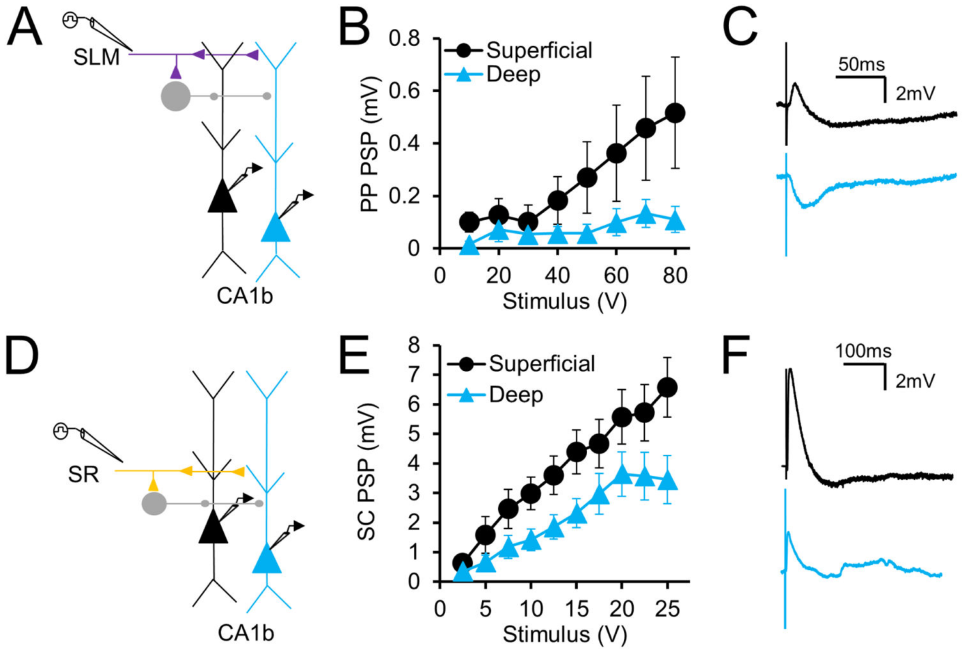

Figure 3. PP excitatory responses are larger in superficial CA1 PNs even in the presence of inhibition in CA1b

(A) Experimental paradigm in which perforant path responses to SLM stimulation are recorded with inhibition intact. (B) Input-output curves of perforant path PSPs in superficial and deep CA1 PNs (n=18 deep,17 superficial). (C) Example perforant path PSPs in superficial (black) and deep (blue) CA1 PNs elicited at 80V (D) Experimental paradigm in which Schaffer collateral responses to SR stimulation are recorded with inhibition intact. (E) Input-output curves of Schaffer collateral PSPs in deep and superficial CA1 PNs (n=22 deep,23 superficial). (F) Example superficial (black) and deep (blue) CA1 PN SC-evoked PSPs elicited at 25 V. Error bars represent ±SEM.

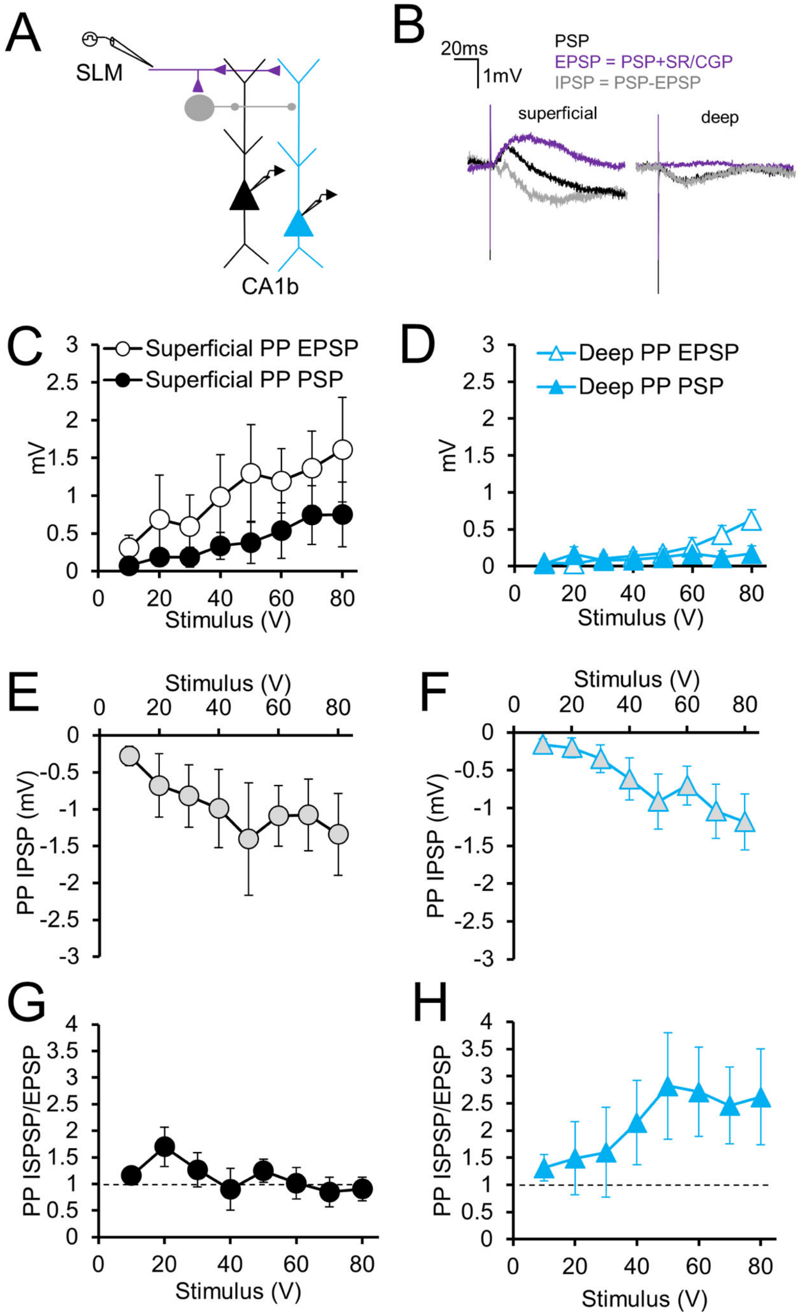

Figure 4. Inhibition evoked by PP stimulation in superficial and deep CA1 PNs of CA1b

(A) Experimental paradigm in which perforant path responses to SLM stimulation are recorded with inhibition intact. (B) Derivation of perforant path IPSP shown in examples of superficial (left) and deep (right) PNs. Perforant path PSP (black) is recorded in control conditions. The EPSP (purple) is generated by the addition of GABAR blockers (SR/CGP). Subtraction of the EPSP from the PSP generates the perforant path IPSP (gray). (C) Input-output curves of perforant path PSPs and EPSPs in superficial CA1 PNs (n=8 each). (D) Input-output curves of perforant path PSPs and EPSPs in deep CA1 PNs (n=8 each). (E) Input-output curve of the derived perforant path IPSP in superficial CA1 PNs (n=8). (F)

Input-output curve of the perforant path derived IPSP in deep CA1 PNs (n=8). (G) Perforant path inhibition-excitation (I/E) ratios in superficial CA1 PNs (n=8). (H) Perforant path I/E ratios in deep CA1 PNs (n=8). Error bars represent ±SEM. See Figure S2 for monosynaptic, direct inhibition.

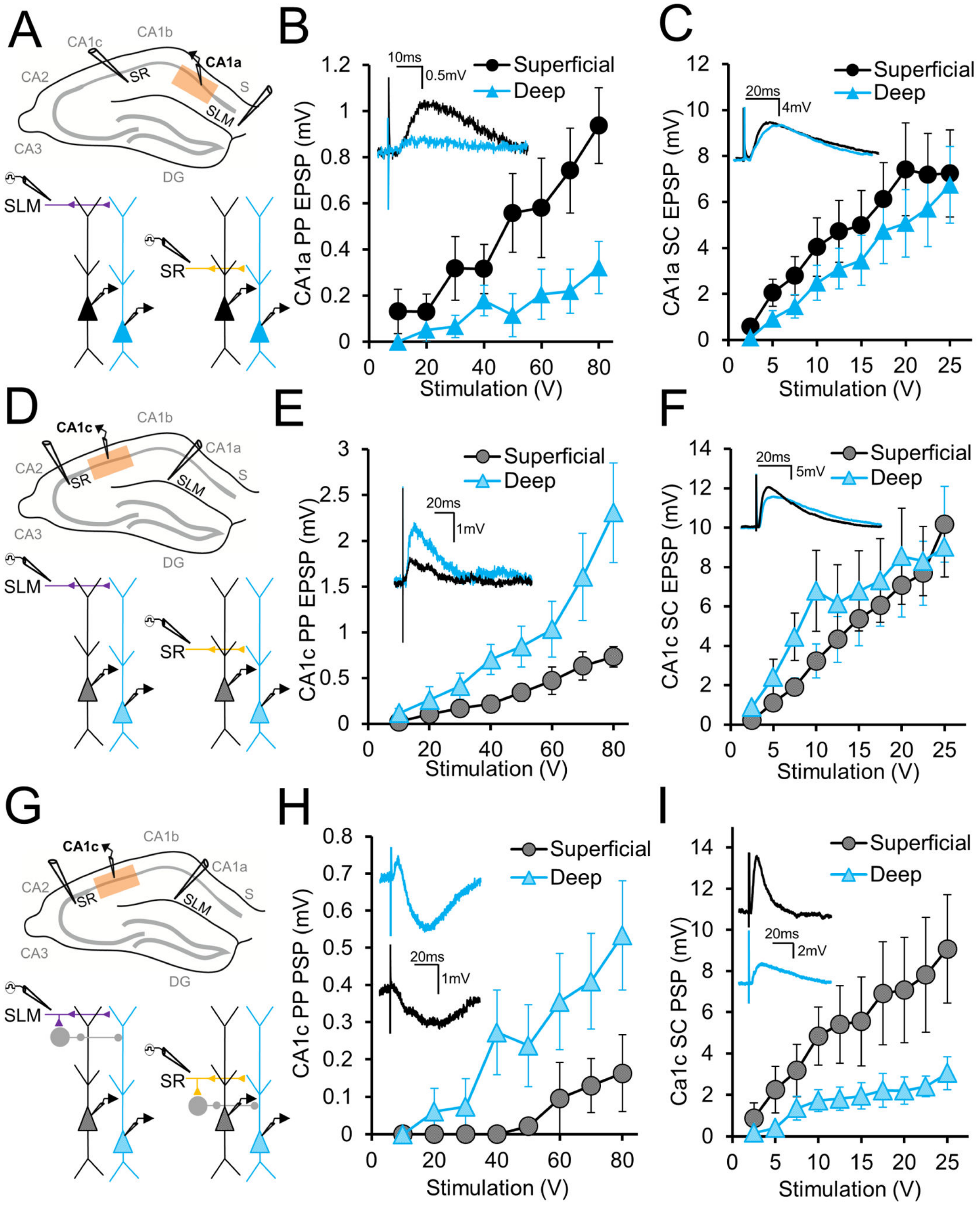

Figure 5. Relative PP synaptic responses in superficial and deep CA1 PNs reverse across the CA1 transverse axis

(A) CA1a area targeted in this experiment (above) and experimental paradigm (below), to record responses to SLM and SR stimulation with inhibition blocked. (B) Input-output curves of perforant path EPSPs elicited in CA1a deep and superficial PNs (n = 10 each) by extracellular SLM stimulation. Examples in inset. (C) Input-output curves of Schaffer collateral EPSPs elicited in CA1a deep and superficial PNs (n = 10 each) by extracellular SR stimulation. Examples in inset. (D) Diagram of CA1c area targeted in this experiment (above) and experimental paradigm (below), to record responses to SLM and SR stimulation with inhibition blocked. (E) Input-output curves of perforant path EPSPs elicited in CA1c deep and superficial PNs (n = 11 each) by extracellular SLM stimulation. Examples in inset. (F) Input-output curves of Schaffer collateral EPSPs elicited in CA1c deep and superficial PNs (n = 11 each) by extracellular SR stimulation. Examples in inset. (G) CA1c area targeted in this experiment (above) and experimental paradigm (below), to record responses to SLM and SR stimulation with inhibition intact. (H) Stimulus response curves of perforant path PSPs elicited in CA1c deep and superficial CA1 PNs (n = 7 each) by extracellular SLM stimulation. Examples in inset. (I) Input-output curves of Schaffer collateral PSPs elicited in CA1c deep and superficial PNs (n = 7 each) by SR stimulation. Examples in inset. Error bars represent ±SEM.

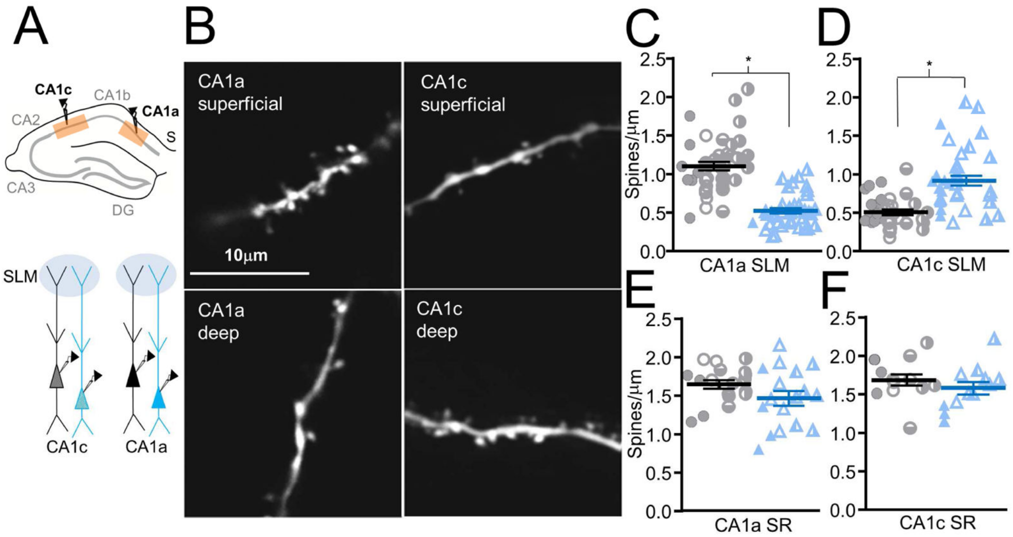

Figure 6. Relative spine density in SLM of deep versus superficial neuron dendrites reverses along the transverse axis

(A) CA1a and CA1c regions targeted for spine density measurement (above and below). (B) Two-photon image of an SLM dendrite of a CA1a superficial PN (upper left), CA1a deep PN (lower left), CA1c superficial PN (upper right), CA1c deep PN (lower right). (C) CA1a SLM dendrite spine densities (sPN: n=42 dendritic branch segments from 4 neurons; dPN: n=37 segments from 4 neurons). (D) CA1c SLM dendrite spine densities (sPN: n=34 dendritic branch segments from 4 neurons; dPN: n=38 segments from 4 neurons). (E) CA1a SR dendrite spines densities (n=18 dendritic branch segments from 4 neurons; dPN: n=17 segments from 4 neurons) (F) CA1c SR dendrite spine densities (sPN: n=12 dendritic branch segments from 4 neurons; dPN: n=12 segments from 4 neurons). For C–F, symbols represent individual dendritic segment with a distinct symbol for each neuron. Horizontal bars represent means (sPN, black; dPN, blue) and error bars represent ±SEM. See Figure S3 for examples of SR dendrite spines.

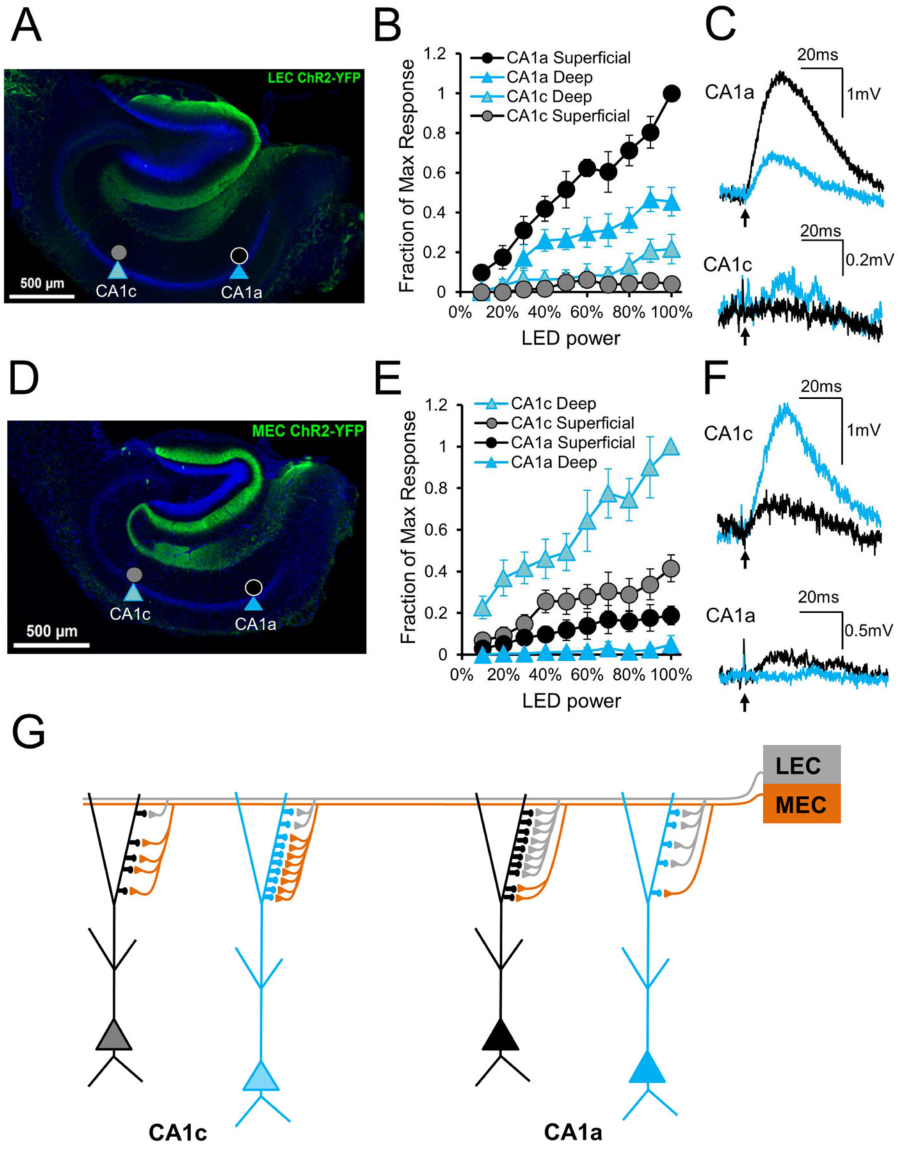

Figure 7. Optogenetic activation of LEC and MEC axons demonstrates preferential activation of CA1 PN subpopulations based on somatic location in radial and transverse axes

(A) EYFP immunohistochemical staining in a 400µm transverse hippocampal slice, from a mouse injected with EYFP-ChR2 in LEC and used for electrophysiology. Targeted PNs are noted. (B) Responses of CA1a and CA1c superficial and deep PNs to a range of LEC axon photostimulation. Responses normalized to the maximum within-slice response, noted in CA1a superficial PNs (n=8 CA1a sPN, 6 CA1a dPN, 7 CA1c sPN, 7 CA1c dPN) (C) Example light-induced LEC EPSPs in CA1a and CA1c superficial (black) and deep (blue) PNs. Large amplitude CA1a traces are single trials; small amplitude CA1c traces are averages of multiple trials. (D) EYFP immunohistochemical staining in a 400µm transverse hippocampal slice, from a mouse injected with EYFP-ChR2 in MEC and used for electrophysiology. Targeted PNs are noted. (E) Responses of CA1a and CA1c superficial and deep PNs to a range of MEC axon photostimulation. Responses normalized to the maximum within-slice response, noted in CA1c deep PNs (n=6 each) (F) Example light-induced MEC EPSPs in CA1a and CA1c superficial (black) and deep (blue) PNs. Large amplitude CA1c traces are single trials; small amplitude CA1a traces are averages of multiple trials. In B, E error bars represent ±SEM. In C, F arrow indicates photostimulation onset. See Figure S4 for unnormalized voltage curves. (G) Proposed EC-CA1 PN connectivity based on the primary findings. MEC drive is strongest towards CA1c whereas LEC drive is strongest towards CA1a. In CA1c, strong MEC and weak LEC input favor deep PNs with more SLM spines. In CA1a, strong LEC and weak MEC input favor superficial PNs with more SLM spines.